JOURNAL OF THE AMERICAN CHEMICAL SOCIETY

Article

pubs.acs.org/JACS

Differentiating Amino Acid Residues and Side Chain Orientations in Peptides Using Scanning Tunneling Microscopy

Shelley A. Claridge,[†,‡,△] John C. Thomas,[†,‡] Miles A. Silverman,[†,‡] Jeffrey J. Schwartz,[†,§] Yanlian Yang,[*,⊥] Chen Wang,[*,⊥] and Paul S. Weiss[*,†,‡,§,¶]

[†] California NanoSystems Institute, University of California, Los Angeles, Los Angeles, California 90095-7227, United States

[‡] Department of Chemistry and Biochemistry, University of California, Los Angeles, Los Angeles, California 90095-7227, United States

[§] Department of Physics and Astronomy, University of California, Los Angeles, Los Angeles, California 90095-7227, United States

[⊥] National Center for Nanoscience and Technology, Beijing 100190, People's Republic of China

[¶] Department of Materials Science and Engineering, University of California, Los Angeles, Los Angeles, California 90095-7227, United States

Supporting Information

ABSTRACT: Single-molecule measurements of complex biological structures such as proteins are an attractive route for determining structures of the large number of important biomolecules that have proved refractory to analysis through standard techniques such as X-ray crystallography and nuclear magnetic resonance. We use a custom-built low-current scanning tunneling microscope to image peptide structures at the single-molecule scale in a model peptide that forms *β* sheets, a structural motif common in protein misfolding diseases. We successfully differentiate between histidine and alanine amino acid residues, and further differentiate side chain orientations in individual histidine residues, by correlating features in scanning tunneling microscope images with those in energy-optimized models. Beta sheets containing histidine residues are used as a model system due to the role histidine plays in transition metal binding associated with amyloid oligomerization in Alzheimer's and other diseases. Such measurements are a first step toward analyzing peptide and protein structures at the single-molecule level.

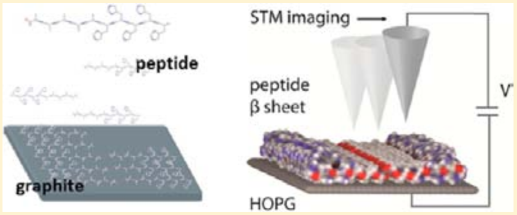

■ INTRODUCTION

The protein data bank now contains tens of thousands of protein structures, most determined by X-ray diffraction (XRD) but with many also resolved by nuclear magnetic resonance (NMR) spectroscopy and small but increasing numbers by electron diffraction.[1] However, substantial challenges remain in understanding important classes of heterogeneous biological structure. These range in scale from transmembrane proteins, including G-protein coupled receptors, which are the targets of half of all commercial pharmaceuticals,[2] to smaller amyloid peptides, including amyloid beta (Aβ), associated with Alzheimer's and other neurodegenerative diseases.[3]

Even relatively simple peptides present characterization challenges when they adopt heterogeneous, noncrystalline structures, a common phenomenon in protein misfolding diseases.[3] For instance, amyloid peptides Aβ_{1-40} and Aβ_{1-42} are cleaved from amyloid precursor protein (APP) and include a section of the APP transmembrane domain that adopts a helical conformation in the protein but instead adopts a *β* sheet conformation in the amyloid plaque.[4] Although it has been possible to crystallize sections of the amyloid peptide for analysis by XRD, current understanding suggests that pathogenicity arises from small, noncrystalline peptide oligomers.[5,6]

Thus, there are substantial advantages to methods for analyzing biological structures in real space, rather than by diffraction, using techniques that do not require large amounts of highly purified molecules. A rapidly growing body of literature highlights the importance of structural and dynamical variations extracted from individual molecules using a variety of techniques.[7−10]

Scanning probe microscopies can provide detailed, label-free structural information for individual molecules on surfaces,[10,11] but certain key limitations have restricted their use in studying biological structure. To date, most biological studies using scanning probes have been based on atomic force microscopy (AFM).[12−18] Although AFM is capable of imaging certain types of small molecules (e.g., pentacene) with remarkably high resolution under special conditions,[19,20] the technique typically lacks the resolution needed to measure subnanometer lateral structures in complex molecules under ambient conditions. For instance, previous images of peptides (including hexaglycylamide[21] and Aβ_{1-42})[17] assembled into *β* sheets on surfaces reveal features characteristic of sheet edges but not structural details within the sheets.

Received: August 18, 2013
Published: November 12, 2013

dx.doi.org/10.1021/ja408550a | *J. Am. Chem. Soc.* 2013, 135, 18528−18535

Scanning tunneling microscopes (STMs) provide higher spatial resolution,[22] but STM images are convolutions of topographic and electronic contributions,[23−25] complicating interpretation of complex structures such as biomolecules comprising multiple functional groups and insulating moieties. Thus, although proteins,[26−29] peptides,[30−40] and other biomolecules[41] assembled on surfaces have been imaged using the STM, distinguishing amino acid side chain conformations in peptides adopting biologically relevant conformations (i.e., β sheets or α helices) has proven challenging. We leverage a custom-built low-noise STM that enables low-current measurements (1−10 pA) under ambient conditions[42,43] in combination with both large-scale molecular modeling and detailed local modeling of electronic structure to investigate peptide backbone conformations and side chain orientations at the single-molecule level.

Here, we image single-molecule structures in a model peptide that forms β sheets, a common protein secondary structural motif relevant to a variety of protein misfolding diseases, including Alzheimer's, Parkinson's, and prion diseases.[44] We have chosen a model peptide (Figure 1) comprising two blocks of five amino acids each. The first block (shown in blue) is composed of histidine residues, which are believed to be important in the context of amyloid aggregation due to formation of complexes between the histidine imidazole side chain and Cu^{2+} and other transition metals.[45,46] Alanine residues (shown in yellow) have methyl side chains; polyalanine expansions are associated with formation of fibrillar peptide aggregates in oculopharyngeal muscular dystrophy.[47]

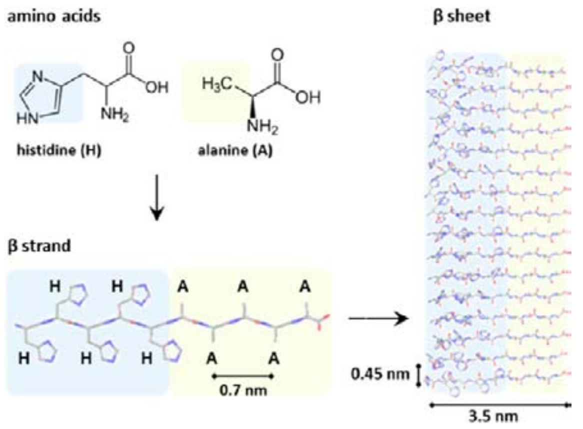

Figure 1. Block polypeptides with sequence HHHHHAAAAA form β sheets based on hydrogen bonding between peptides. In each β strand, amino acid side chains are exposed on alternating faces of the β sheet. Solutions of the peptide self-assemble on highly oriented pyrolytic graphite (HOPG) into lamellar structures composed of aligned β sheets.

■ EXPERIMENTAL METHODS

Materials. HPLC-grade acetonitrile (Sigma-Aldrich, St. Louis, MO) was used as received. Custom peptides with sequences HHHHHAAAAA and HHHHHFFFFFHHHHH were purchased from CS Bio (Menlo Park, CA) and prepared as described below. Highly oriented pyrolytic graphite (HOPG), grade ZYA (SPI Supplies, West Chester, PA), was cut into pieces of suitable size for the sample holder in the custom STM and then freshly cleaved prior to use. Pt/Ir wire with a diameter of 0.25 mm (Goodfellow, Oakdale, PA) was used to prepare STM tips. For PM-IRRAS measurements, an HOPG monochromator, grade ZYB, 25 mm × 40 mm × 2 mm from Momentive Performance Materials (Strongsville, OH) was used.

Sample Preparation. Peptide assemblies were formed on HOPG substrates (SPI Supplies, grade ZYA) with typical dimensions of 5 mm × 5 mm, which were freshly cleaved prior to deposition. Peptides were dissolved in a 1:1 (vol:vol) mixture of double-distilled water (ddH_2O) and acetonitrile, to a final peptide concentration of 0.01−0.1 mg/mL, immediately prior to use. Peptide solution was drop cast (approximately 20 μL) on the freshly cleaved HOPG and incubated at room temperature for 10−30 s. Excess solvent was blown off the surface using ultrapure nitrogen gas.

STM Measurements. All STM measurements were performed using custom Besocke-style STMs designed to enable low-current measurements under ambient conditions due to the short signal path between the tunneling junction and the current−voltage conversion in the high-sensitivity Axon CV-4 preamplifier.[42,48−50] Measurements were performed either under ambient or cryogenic (77 K) ultrahigh vacuum ($<10^{-10}$ Torr) conditions,[51] as noted in the manuscript. Pt/Ir STM tips were mechanically prepared.

AFM Measurements. All AFM measurements were performed under ambient conditions using a Bruker Dimension 5000 instrument in tapping mode with Nanoprobe (Neuchatel, Switzerland) PPP-FM tips (nominal force constant 2.8 N/m and radius of curvature <10 nm).

Circular Dichroism Measurements. Circular dichroism spectroscopy measurements were performed using a JASCO (Easton, MD) J-715 Circular Dichroism Spectrophotometer. Peptide solutions were measured as prepared for surface adsorption measurements using a cell with a 2 mm path length. Spectra were recorded with a step resolution of 0.5 nm, scan speed of 20 nm/min, bandwidth of 1 nm, and sensitivity of 20 mdeg ellipticity, with four spectra collected and averaged per sample.

Polarization Modulation Infrared Reflection Absorption Spectroscopy (PM-IRRAS) Measurements. PM-IRRAS measurements were performed using a Nicolet Fourier transform infrared (FTIR) spectrometer (Thermo Electron Corp., Waltham, MA) equipped with a liquid-nitrogen-cooled mercury−cadmium−telluride detector and a Seagull variable-angle reflection accessory (Harrick Scientific Inc., Pleasantville, NY). Measurements were performed in a controlled atmosphere chamber purged with dry N_2 for at least 30 min prior to spectrum acquisition. Spectra were collected at the grazing incidence angle (75° relative to the surface normal) and a mirror speed of 1.27 cm/s with a resolution of 2 cm^{-1}.

Molecular Modeling. Model β-strand peptides were generated using MOLEMAN2 software (Uppsala). Low-energy rotamers of side chains were calculated using PyRosetta, and MacroModel software (Schrödinger, Cambridge, MA) was used to model the binding of a sheet comprised of a 16 × 2 array of β strands to an atomically flat graphite surface.

Structures were minimized in MacroModel using the Polak−Ribiere conjugate gradient (PRCG) method with a convergence threshold of 0.05. The graphite surface was constrained during modeling, and structures were minimized in the absence of solvents. An OPLS_2005 force field was used, and normal cutoffs for van der Waals, electrostatic, and hydrogen-bonding interactions were set.

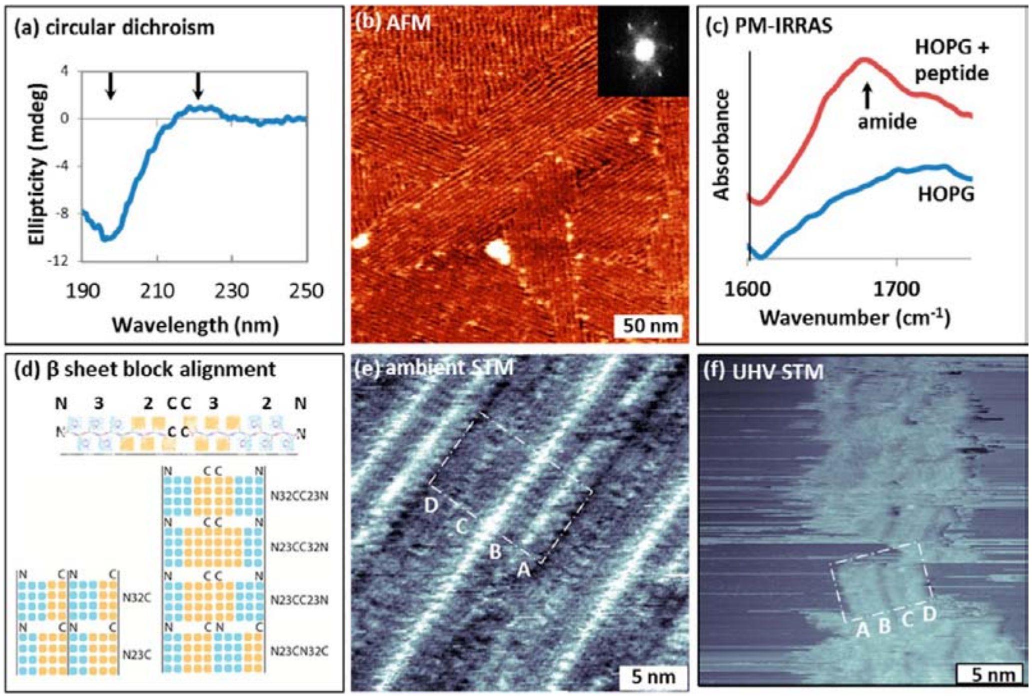

Figure 2. (a) Circular dichroism spectrum of HA peptides in solution. (b) AFM image (and Fourier transform, inset) of HA peptides on HOPG showing lamellar widths of 3.57 nm (compared with 3.50 nm expected width for an ideal β sheet). (c) Polarization-modulated infrared reflection absorption spectrum of HA assembled on HOPG with amide I peak characteristic of β sheet formation. (d) Models of possible alignments of adjacent β sheets highlighting N32CC32N alignment observed in (e) and (f). (e) Ambient STM image of HA on HOPG (I_{tunnel} = 6 A, V_{sample} = 0.5 V). (f) UHV-STM image (I_{tunnel} = 15 pA, V_{sample} = −1.0 V) of single peptide lamella on HOPG exhibiting streak characteristics due to weakly bound adsorbate molecules being dragged by the STM tip.

Frontier orbitals for simplified peptide structures (paired alanine trimers on a small graphite surface) were modeled in Gaussian 09 using a B3LYP/6-31G basis set.

RESULTS

The β strands assemble side by side on the highly oriented pyrolytic graphite (HOPG) surface through hydrogen bonding to form β sheets in which amino acid side chains are alternately exposed on opposite sides of the sheet along the length of each strand.[52] In an idealized β strand, the distance between side chains is 0.7 nm along the peptide, with a 0.45 nm interchain spacing between peptides in the sheet, although biologically these values can vary substantially and are dependent on side chain conformations. The β strands may hydrogen bond in either parallel or antiparallel conformations; although the antiparallel conformation is more common in biological structures resulting from intrastrand hydrogen bonding, parallel conformations are also widely observed, particularly in amyloid fibrils,[5,6,53] and appear to be formed by the peptides used here, presumably because this structure allows for π-stacking and hydrogen-bonding interactions between histidine groups on adjacent chains.

When such peptides adsorb to the atomically flat HOPG surface used in our measurements, the zigzag geometry of the β strand backbone produces a configuration in which one-half of the amino acid side chains are adsorbed to the surface, leaving the other half exposed on the upper face of the sheet. The distance between hexagon centers in the graphite lattice is 0.246 nm, meaning alternate side chains along one face of an ideal β strand can register with every third hexagon center with a mismatch of approximately 5%. Because side chains in the model peptides used here are methyl groups (for alanine) and heteroaromatic rings (for histidine), a combination of van der Waals and π-stacking interactions are expected with the graphite surface.[54] Peaks near 195 and 220 nm in the circular dichroism spectra (Figure 2a) indicate that the peptides adopt a random coil conformation in solution and assemble in the presence of the HOPG surface. Such structural transitions at hydrophilic−hydrophobic interfaces are especially relevant to amyloid oligomerization in which one mechanism of cytotoxicity is believed to involve formation of β motifs that disrupt ionic homeostasis across the cell membrane.[55]

We image the assembled peptides by AFM in tapping mode under ambient conditions to observe surface topography using a cantilever with a low force constant (nominally 2.8 N/m) and small radius of curvature (<10 nm) to achieve high spatial resolution in the flat layer of relatively soft peptide on HOPG. The AFM images (Figure 2b) reveal β sheets aligned to form lamellar structures with domains at approximately 120° angles, consistent with previous reports of such peptides[17,40] assembling epitaxially with the HOPG hexagonal lattice (see Supporting Information for AFM and STM images at HOPG step edges). Close observation reveals small deviations from 120° at some boundaries, consistent with the fact that in some domains, peptides tilt relative to the lamellar axis, a phenomenon currently under investigation in the context of its energetic consequences for hydrogen bonding between peptides.

Lamellar widths are commensurate with calculated values for peptides adopting β sheet conformations (Figure 2b and Supporting Information), 3.6 nm for sheets formed from 10-amino-acid peptides (vs 3.5 nm expected for an ideal β sheet) and 5.0 nm for sheets formed from 15-amino-acid peptides (vs 5.25 nm for an ideal β sheet). Atomic step edges in the graphite

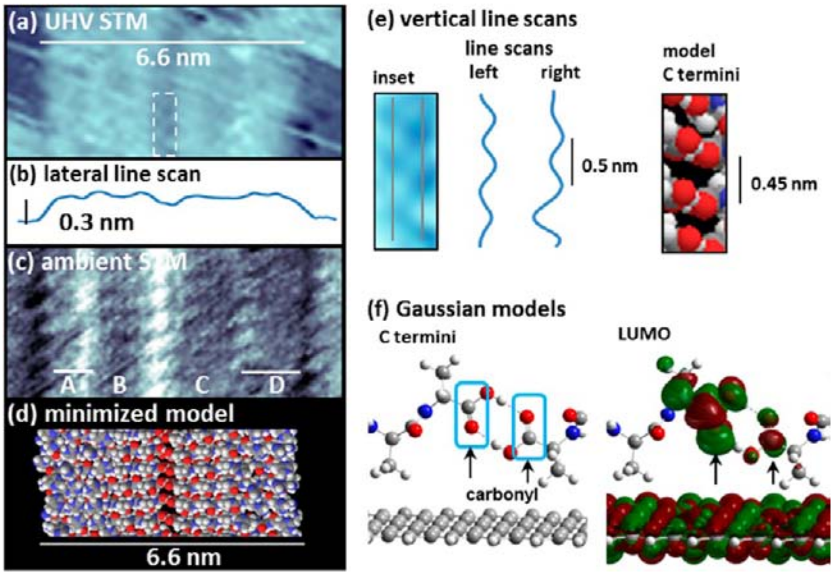

Figure 3. Structural analysis of HA lamellar features. (a) Inset from UHV-STM image in Figure 2f showing 6.6-nm double-lamellar width. (b) Lateral line scan showing lamellar profile. (c) Inset from ambient STM image in Figure 2e showing symmetry with UHV image and contrast difference in feature near center. (d) Energy-minimized model of HA peptides on graphite showing alignment of peptide termini and block boundaries with images above. (e) Analysis of peptide interchain spacing based on features in inset from (a), including line scans and comparison with appropriate region of model in (d). (f) Modeling of frontier orbitals in paired alanine oligomers on HOPG showing the LUMO extends most prominently from the surface just above the carbonyl to the left (highlighted with the blue boxes and arrow, left, and arrow, right), consistent with the high-intensity feature in the image.

surface (0.34 nm) are also apparent and are large relative to the local height variations within individual lamellae (see Supporting Information). At higher concentrations of HA, irregular 1−5 nm peptide aggregates also appear at domain boundaries (Figure 2b). Polarization-modulated infrared reflection absorption (PM-IRRAS) measurements reveal a peak at 1696 cm^{-1} characteristic of β sheet formation (Figure 2c).

Imaging peptides with the STM provides higher spatial resolution because of both the sharpness of the STM probe tip and the exponential decay of the tunneling current with increasing tip−sample distance. In large-scale ambient STM measurements of the same peptide (Figure 2e), epitaxially aligned domains are also visible, similar in overall structure to those in AFM images (Figure 2b). Peptides are imaged using an ultrastable STM under ultrahigh vacuum (UHV) conditions (10^{-12} Torr) and at low temperature (77 K) in order to measure lamellar dimensions accurately (Figure 2f). Under these conditions, the measured double lamellar width is 6.6 nm, in agreement with the width of the structure in the energy-optimized model. Interchain distances are measured based on the repeat distances of features along the central axis, with measured values of 0.5 nm, again in agreement with the distribution of interchain distances observed in minimized models, near the value of 0.45 nm in an ideal β sheet. Line scans across the lamella show an apparent height of 0.3 nm, less than the modeled geometric structure height of 0.9 nm; this result is expected, since STM images typically underestimate heights for insulating species due to relatively weak mixing of the molecular HOMO and LUMO levels and substrate orbitals near the Fermi level.[56,57] Streaking is evident throughout the image, characteristic of weak molecule−substrate interactions such as those between peptides and HOPG. Single-point energy calculations based on OPLS-2005 force fields yield molecule−substrate adsorption energies of approximately 120 kJ/mol, smaller than calculated interaction energies for peptides within the β sheet (∼420 kJ/mol). Contrast variations are evident within the lamellar structure, corresponding to topographic and electronic features along the length of the pairs of peptides.[56,58,59] Four textural domains are visible across the width of the lamellae (Figure 2e, labeled A−D), as well as a high-intensity feature that is visible near the center of each lamella and a varying high-intensity feature to the right. Note that, although higher resolution is typically achieved in STM images recorded in UHV, the lamellar structure is not stabilized by interactions with adjacent lamellae here, somewhat reducing the apparent resolution of the structure found in Figure 2f in comparison with the ambient STM image in Figure 2e. The STM scans mechanically and slowly compared to molecular motions. If molecules or parts of molecules in the tunneling junction move on the time scale of imaging, either thermally or through interactions with the probe tip, their positions are averaged and effectively blurred.[60,61]

Regions near the center of the lamellae (Figure 2e, regions B and C), on both sides of the high-intensity stripe, have regular structures, whereas both edges of the lamellae (Figure 2e, regions A and D) have less regular textures, quantified using entropy metrics in MATLAB. When entropy in gray scale values is measured for regions 9 pixels across, centered at each pixel, mean entropy values are 18% higher for regions at the lamellar edge than for the central region (see Supporting Information). Each peptide is composed of a diblock structure comprising one histidine block and one alanine block; thus, the four textural blocks observed across the lamellar width can be understood to represent differences in side chain structure and orientation along two peptide chains. The alanine methyl side chain has fewer possible conformations than the imidazole side chain of the histidine. This suggests that the two exterior zones (Figure 2e, regions A and D) are the histidine blocks and that variations in side chain orientation lead to the variable block

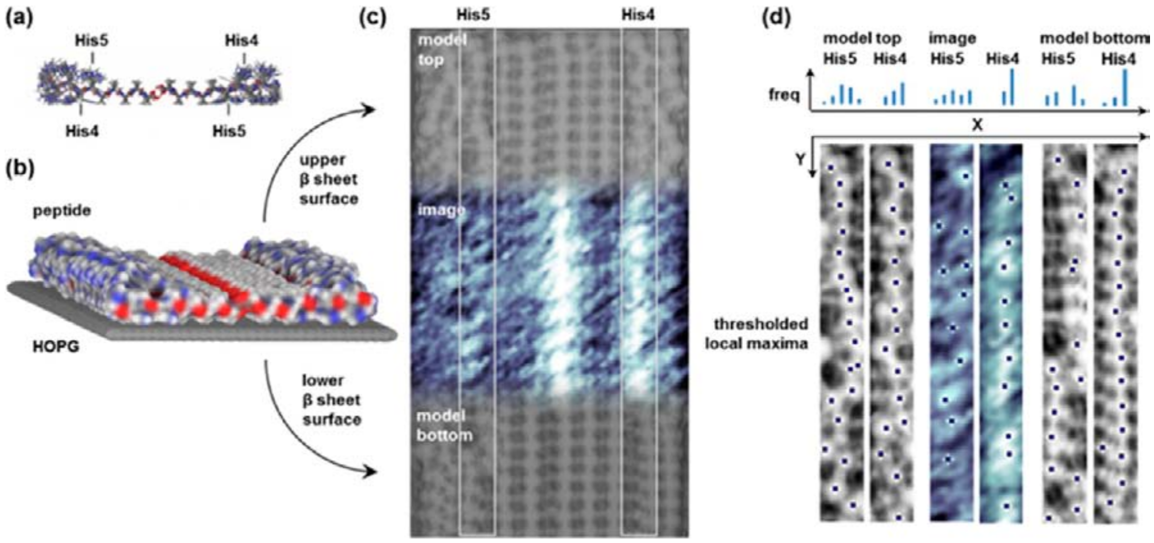

Figure 4. Correlating features in an STM image of self-assembled HA peptides with structure in an energy-optimized model of the HA peptides on HOPG suggesting that under these conditions, structural features in the STM image arise from the structure on the top face of the peptide sheet. (a) Side view of model HA peptide sheet on HOPG highlighting rows of histidine residues at the block boundaries. (b) Model of peptide sheet binding to HOPG surface, resulting in differences between top and bottom faces, distinguishable in models and STM images. (c) STM image and models of top and bottom peptide sheet surfaces highlighting modeled and observed surface features at block boundaries. (d) Histograms and images showing automatically detected lateral peak positions for highlighted rows in top and bottom faces of model and STM image (see Supporting Information for full image regions sampled).

texture, in agreement with molecular surfaces generated from energy-optimized models of β sheets of the peptide (Figure 3d).

To facilitate comparison of structures visible in Figure 2e and f, representative blocks (highlighted with dashed white lines) are enlarged (Figure 3a and c) and aligned with a molecular model (Figure 3d). Note that the region from Figure 2e (enlarged in Figure 3c) has been rotated ~150° clockwise to match the textural regions in Figure 2f (enlarged in Figure 3a). The molecular model in Figure 3d is a top-down view showing six pairs of peptides, and is a subset of a larger model used for energy minimization, containing 32 peptides.

Assigning the blocks as shown in Figure 3c would mean that the paired peptides align head-to-head with their alanine regions at the center of the lamellae. If high percentages of the carboxyl termini are in their neutral form, likely under the solution conditions (1:1 mixture of ddH_2O and acetonitrile, which increases the pK_a of acidic protons[62]), pairs of hydrogen bonds can form between the carboxyl groups, stabilizing this configuration by ~20 kJ/mol on the basis of the energy-minimized model above.

The position of the high-intensity feature near the center of the peptide sheet corresponds to the paired carboxyl termini of the peptide sheets (red feature in center of molecular model, Figure 3d). Interestingly, previous STM images of monolayers of carboxy-terminated alkanethiols on HOPG have not exhibited high-intensity features corresponding to the carboxylic acid group.[56] However, in those monolayers, both experimental evidence and modeling pointed to carboxyl groups oriented parallel to the HOPG surface.[56,58] Here, modeling predicts that the carbonyl groups will be oriented nearly normal to the graphite (Figure 3d), altering the orientations of orbitals in the carbonyls. Note that in Figure 3a, the contrast of the central feature is reversed, consistent with assignment as an electronic rather than a topographic feature. Such contrast reversals are often observed in STM images and are typically associated with small differences in the electronic structure of the STM tip that modulate tunneling behavior and, thus, are not necessarily correlated with structural changes in the molecule.[63]

However, the position of these features can be used to deduce information about the molecular structure and orientation. The locations of the high-intensity features slightly off-axis suggest that they are each aligned with just one of the terminal carbonyl groups rather than both. On the basis of the modeled structural alignment with the STM image, the feature is correlated with the carbonyl group to the right, in which the carbon atom is proximal to the STM tip. Electronic structure modeling in Gaussian[64] using a simplified peptide dimer oriented on an HOPG surface supports this assignment because the first two unoccupied orbitals with density on the molecule lie primarily on this carbonyl group (Figure 3f).

The zigzag peptide backbone structure in the β sheet results in two chemically distinct faces on each sheet: one exposes two histidine (His) side chains and three alanine (Ala) side chains, with the fourth histidine residue His4 at the block boundary; the other exposes three histidines and two alanines, with His5 at the block boundary. Thus, if the textural differences are due to physical differences in the amino acid side chains, the differences can in principle be used to determine the relative orientations of the two sheets. Closer examination reveals that the histidine region on the left edge of the lamellae (Figure 2d, region A) is wider than the region at the right edge (region D) by a ratio of approximately 3:2 (highlighted by a pair of lines above the region labels). This ratio is consistent with the paired sheet conformation shown in Figure 3d, in which three histidine side chains in the left sheet and two in the right sheet are visible. Re-examining Figure 2e in light of this assignment shows the adjacent lamellae adopt the same conformation, supporting the hypothesis that the structure is energetically stable.

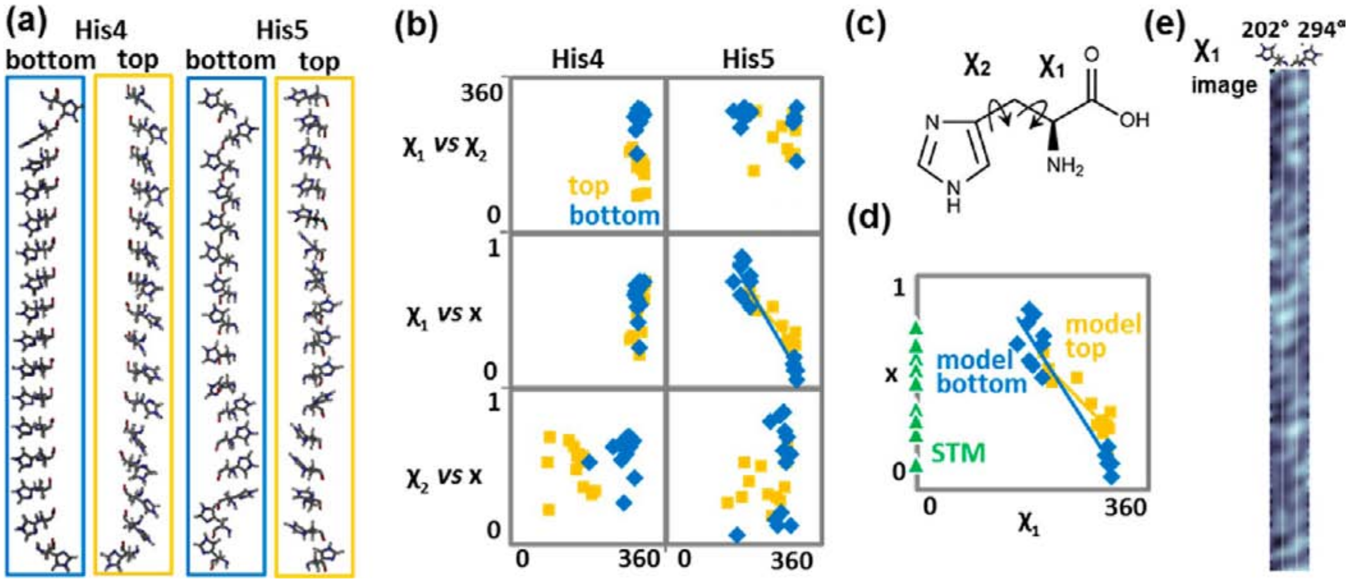

Figure 5. (a) Differences in peak position corresponding to differences in amino acid side chain rotational angles χ_1 and χ_2. (b) Best-fit lines that are calculated for the correlation between χ_1 and peak position x, which allows rotational angle to be calculated for peaks in the image. (c) Schematic showing rotational angles χ_1 and χ_2 for histidine. (d) Distribution of x values from STM image (green) relative to distributions of x values for model top (yellow) and bottom (blue). (e) Correlation of peak position in STM image to the two χ_1 rotamer orientations. Vertical white lines at the expected peak positions are overlaid as a guide to the eye.

Textural differences establish the sheet orientations relative to each other but do not necessarily reveal their orientation relative to the surface because STM contrast arises from tunneling through molecular orbitals and into surface orbitals modulated by the molecule binding to the surface.[23,56,65,66] In this case, both upper and lower faces of the two-sheet structure contain one His5 and one His4 boundary (Figure 4a).

However, optimized models of the peptide sheets binding to the HOPG surface elucidate small but distinctive differences in side chain orientations at the upper and lower interfaces that may be used to distinguish which interface produces contrast in the STM image (Figure 4b). To correlate features in STM images with physical structures in the model, we generate a molecular surface based on the model and then use simple thresholding to identify peaks automatically in both the upper and lower faces of the peptide sheets as well as in the STM images (Figure 4d). Thresholding in STM images enables analysis of peak positions at both high- and low-intensity boundary regions based on apparent height differences with surrounding pixels.

Examining the interior edges of the histidine blocks on the upper and lower faces of the model shows characteristic differences in the peak position distributions at the four boundaries (Figure 4d, histograms). On the bottom face, a single peak position dominates at the His4 boundary (right), whereas two peak positions are found at the His5 boundary (left). Note that in Figure 4c, the bottom surface model has been reoriented relative to the models in Figure 4a and 4b, in order to align the His5 and His4 boundaries with those in the image. On the top face, at both His4 and His5 boundaries, similar preferred peak positions are evident, although there is a greater distribution in the peaks. Such a distribution is expected because side chains on the top face have increased steric freedom relative to those on the bottom face, which are constrained by the proximity of the HOPG surface.

Comparing the peak position histograms for the His4 and His5 boundary regions in the STM image with those in the model helps establish which face of the peptide sheet provides the principal contrast in the image. Note that the small amount of noise in the STM image necessitates more stringent thresholding in peak selection, and as a result, a slightly longer area is sampled to acquire the same number of peaks for the histograms. Figure 4d shows a subset of the length cropped to match the model in scale; for the full image sampled, see Supporting Information.

Both top and bottom model His4 boundaries have single peak distributions that are strongly skewed to the right, matched by the histogram for the image His4 boundary. However, at the His5 boundary, the image's His5 peaks more closely match the characteristics of the model top His5 boundary, with a single distribution of peaks across the lane width. The model bottom His5 boundary, in contrast, has two clusters of peaks on opposite sides of the lane. This result suggests that under these conditions, STM image contrast arises primarily from the top face of the peptide. Such an assignment is additionally supported by the variable contrast in the histidine regions away from the boundary rows, consistent with the more highly varied top surface of the molecular model. We note that this top-surface sensitivity of topographic STM images is also found for self-assembled monolayers of alkanethiols.[67] With other STM modalities, such as local barrier height imaging, it is possible to achieve contrast of buried layers and interfaces.[67]

Variations in molecular surface topography at the His4 and His5 boundaries are due to differences in rotational orientation of the imidazole side chains (Figure 5a). Rotation in amino acid side chains is quantified in terms of χ_1 and χ_2 values (Figure 5c), with χ_1 describing the rotation of the carbon−carbon single bond branching from the peptide backbone and χ_2 describing the rotation of the bond to the remainder of the side chain (in histidine, the imidazole ring). In the optimized peptide models here, two populations of histidine rotamers with mean χ_1 values of 202° and 294° are found (Figure 5b, top), in agreement with two common rotamers for histidine observed in β sheets.[68]

Note that although χ values are typically reported with values in the range (−180°, 180°), here we offset the negative interval (−180°, 0°) by 360°, instead reporting equivalent values in the range 0° to 360°. This facilitates analysis of the rotamer population around $\chi_1 = 202°$, which otherwise appears as two groups near −180° and 180°.

At the His4 boundary, the $\chi_1 = 294°$ rotamer is strongly favored, but at the His5 boundary where both rotamers are found, the peak position x correlates with χ_1 (Figure 5b, middle right). This correlation can be used to differentiate between $\chi_1 = 202°$ and $\chi_1 = 294°$ rotamers in the STM image (Figure 5e). Within each rotamer population, there is a distribution of peak positions and intensities; this result is expected based on differences in the χ_2 rotation angle on the top face of the sheet, which can change both the position and the topographic height of the imidazole ring. Note that on the bottom face of the sheet, modeled χ_2 values have a different mean and a reduced standard deviation as the imidazole rings twist to optimize π-stacking with the surface, resulting in values of 265 ± 27° in contrast to values of 196 ± 58° for equivalent rows on the top face (see Supporting Information). In the STM image, it is possible that differences in intensity may also be influenced by changes in the epitaxy between the peptide and the graphite surface along the length of the sheet, although this would typically be visible as a periodic Moiré pattern,[56] whereas the variations in these regions appear less regular.

Even on the more variable top face, values of χ_1 are correlated in adjacent chains, with median differences of 14.9° and 9.8° for His4 and His5 boundaries, respectively, suggesting short-range steric or electronic interactions between imidazole groups. The ability to observe such correlations may be biologically useful since π-stacking is one of the key interactions believed to drive the formation of amyloid peptides.[45]

■ CONCLUSIONS AND PROSPECTS

Differentiating between amino acid residues and between individual amino acid side chain orientations in a disease-relevant peptide structural motif is a first step toward determining heterogeneous peptide and protein structures at the single-molecule level without requiring crystallization. In particular, the ability to observe side chain orientations in histidine imidazole rings would be important in characterizing transition metal binding associated with amyloid oligomerization and cytotoxicity in a variety of neurodegenerative diseases. A generalized interpretation of biological structure (including both structural elements such as α helices and more complex structural elements such as amyloid cross-β motifs) based on STM imaging will require more extensive chemical imaging capabilities, as well as the ability to address both exposed and buried interfaces in molecules, and ultimately the capability to image structures in solution. Ongoing experiments seek to address these concerns in the context of self-assembling biomolecular structures, using a new suite of custom instruments designed to extract additional image data channels from molecules assembled on surfaces.[66,69] Use of other 2D layered materials such as MoS_2 as substrates will allow substrate lattices to be varied, modulating contact with the biomolecular assembly. The method can also be applied to other conductive surfaces (e.g., metals) that form covalent bonds to biomolecules to facilitate stable sample alignment.

■ ASSOCIATED CONTENT

Ⓢ Supporting Information

Atomic force microscopy measurements of lamellar width, MATLAB textural analysis, histograms of χ_1 and χ_2 values. This material is available free of charge via the Internet at http://pubs.acs.org.

■ AUTHOR INFORMATION

Corresponding Author

yangyl@nanoctr.cn; wangch@nanoctr.cn; psw@cnsi.ucla.edu

Present Address

△Department of Chemistry and Department of Biomedical Engineering, Purdue University, West Lafayette, Indiana 47907, United States

Author Contributions

The manuscript was written through contributions of all authors. All authors have given approval to the final version of the manuscript.

Notes

The authors declare no competing financial interest.

■ ACKNOWLEDGMENTS

We thank Dr. Lukasz Goldschmidt and Prof. David Eisenberg for helpful discussions and DoE (DE-SC0005161), NIH (NRSA postdoctoral fellowship, S.A.C.), the Merkin Family Foundation (S.A.C.), and the Kavli Foundation (P.S.W.) for financial support. We also gratefully acknowledge the use of the scanning probe microscopy facility at the Nano and Pico Characterization Lab at the California NanoSystems Institute.

■ REFERENCES

(1) Lacapere, J. J.; Pebay-Peyroula, E.; Neumann, J. M.; Etchebest, C. *Trends Biochem. Sci.* **2007**, *32*, 259.

(2) Howard, A. D.; McAllister, G.; Feighner, S. D.; Liu, Q. Y.; Nargund, R. P.; Van der Ploeg, L. H. T.; Patchett, A. A. *Trends Pharmacol. Sci.* **2001**, *22*, 132.

(3) Aguzzi, A.; O'Connor, T. *Nat. Rev. Drug Disc.* **2010**, *9*, 237.

(4) Barrett, P. J.; Song, Y.; Van Horn, W. D.; Hustedt, E. J.; Schafer, J. M.; Hadziselimovic, A.; Beel, A. J.; Sanders, C. R. *Science* **2012**, *336*, 1168.

(5) Chiti, F.; Dobson, C. M. *Annu. Rev. Biochem.* **2006**, *75*, 333.

(6) Luca, S.; Yau, W. M.; Leapman, R.; Tycko, R. *Biochem.* **2007**, *46*, 13505.

(7) Moerner, W. E. *J. Phys. Chem. B* **2002**, *106*, 910.

(8) Weiss, S. *Science* **1999**, *283*, 1676.

(9) Bustamante, C.; Bryant, Z.; Smith, S. B. *Nature* **2003**, *421*, 423.

(10) Claridge, S. A.; Schwartz, J. J.; Weiss, P. S. *ACS Nano* **2011**, *5*, 693.

(11) Giessibl, F. J. *Rev. Mod. Phys.* **2003**, *75*, 949.

(12) Hansma, H. G.; Hoh, J. H. *Annu. Rev. Biophys. Biomol. Struct.* **1994**, *23*, 115.

(13) Rief, M.; Gautel, M.; Oesterhelt, F.; Fernandez, J. M.; Gaub, H. E. *Science* **1997**, *276*, 1109.

(14) Engel, A.; Muller, D. J. *Nat. Struct. Biol.* **2000**, *7*, 715.

(15) Fisher, T. E.; Marszalek, P. E.; Fernandez, J. M. *Nat. Struct. Biol.* **2000**, *7*, 719.

(16) Ando, T.; Kodera, N.; Takai, E.; Maruyama, D.; Saito, K.; Toda, A. *Proc. Natl. Acad. Sci. U. S. A.* **2001**, *98*, 12468.

(17) Arimon, M.; Diez-Perez, I.; Kogan, M. J.; Durany, N.; Giralt, E.; Sanz, F.; Fernandez-Busquets, X. *FASEB J.* **2005**, *19*, 1344.

(18) Greenleaf, W. J.; Woodside, M. T.; Block, S. M. *Annu. Rev. Biophys. Biomol. Struct.* **2007**, *36*, 171.

(19) Gross, L.; Mohn, F.; Moll, N.; Liljeroth, P.; Meyer, G. *Science* **2009**, *325*, 1110.

(20) Gross, L. *Nat. Chem.* **2011**, *3*, 273.

(21) Prokhorov, V. V.; Klinov, D. V.; Chinarev, A. A.; Tuzikov, A. B.; Gorokhova, I. V.; Bovin, N. V. *Langmuir* **2011**, *27*, 5879.
(22) Hansma, P. K.; Tersoff, J. *J. Appl. Phys.* **1987**, *61*, R1.
(23) Eigler, D. M.; Weiss, P. S.; Schweizer, E. K.; Lang, N. D. *Phys. Rev. Lett.* **1991**, *66*, 1189.
(24) Hofer, W. A.; Foster, A. S.; Shluger, A. L. *Rev. Mod. Phys.* **2003**, *75*, 1287.
(25) Tersoff, J.; Hamann, D. R. *Phys. Rev. B* **1985**, *31*, 805.
(26) Arakawa, H.; Umemura, K.; Ikai, A. *Nature* **1992**, *358*, 171.
(27) Friis, E. P.; Andersen, J. E. T.; Madsen, L. L.; Moller, P.; Ulstrup, J. *J. Electroanal. Chem.* **1997**, *431*, 35.
(28) Chi, Q. J.; Zhang, J. D.; Nielsen, J. U.; Friis, E. P.; Chorkendorff, I.; Canters, G. W.; Andersen, J. E. T.; Ulstrup, J. *J. Am. Chem. Soc.* **2000**, *122*, 4047.
(29) Zhang, J. D.; Welinder, A. C.; Chi, Q. J.; Ulstrup, J. *Phys. Chem. Chem. Phys.* **2011**, *13*, 5526.
(30) Breen, J. J.; Flynn, G. W. *J. Phys. Chem.* **1992**, *96*, 6825.
(31) Senn, H. M.; Thiel, W. *Angew. Chem., Int. Ed.* **2009**, *48*, 1198.
(32) Mao, X. B.; Ma, X. J.; Liu, L.; Niu, L.; Yang, Y. L.; Wang, C. *J Struct. Biol.* **2009**, *167*, 209.
(33) Mao, X. B.; Wang, C. X.; Ma, X. J.; Zhang, M.; Liu, L.; Zhang, L.; Niu, L.; Zeng, Q. D.; Yang, Y. L.; Wang, C. *Nanoscale* **2011**, 3, 1592.
(34) Matmour, R.; De Cat, I.; George, S. J.; Adriaens, W.; Leclere, P.; Bomans, P. H. H.; Sommerdijk, N. A. J. M.; Gielen, J. C.; Christianen, P. C. M.; Heldens, J. T.; van Hest, J. C. M.; Lowik, D. W. P. M.; De Feyter, S.; Meijer, E. W.; Schenning, A. P. H. J. *J. Am. Chem. Soc.* **2008**, *130*, 14576.
(35) Sek, S.; Xu, S.; Chen, M.; Szymanski, G.; Lipkowski, J. *J. Am. Chem. Soc.* **2008**, *130*, 5736.
(36) Deng, Z.; Thontasen, N.; Malinowski, N.; Rinke, G.; Harnau, L.; Rauschenbach, S.; Kern, K. *Nano Lett.* **2012**, *12*, 2452.
(37) Kalashnyk, N.; Nielsen, J. T.; Nielsen, E. H.; Skrydstrup, T.; Otzen, D. E.; Laegsgaard, E.; Wang, C.; Besenbacher, F.; Nielsen, N. C.; Linderoth, T. R. *ACS Nano* **2012**, *6*, 6882.
(38) Hohman, J. N.; Kim, M.; Wadsworth, G. A.; Bednar, H. R.; Jiang, J.; LeThai, M. A.; Weiss, P. S. *Nano Lett.* **2011**, *11*, 5104.
(39) Wang, C.; Mao, X.; Yang, A.; Niu, L.; Wang, S.; Li, D.; Guo, Y.; Wang, Y.; Wang, C. *Chem. Commun.* **2011**, *47*, 10638.
(40) Liu, L.; Zhang, L.; Niu, L.; Xu, M.; Mao, X. B.; Yang, Y. L.; Wang, C. *ACS Nano* **2011**, *5*, 6001.
(41) Kim, Y.; Long, E. C.; Barton, J. K.; Lieber, C. M. *Langmuir* **1992**, *8*, 496.
(42) Bumm, L. A.; Weiss, P. S. *Rev. Sci. Instrum.* **1995**, *66*, 4140.
(43) Moore, A. M.; Yeganeh, S.; Yao, Y. X.; Claridge, S. A.; Tour, J. M.; Ratner, M. A.; Weiss, P. S. *ACS Nano* **2010**, *4*, 7630.
(44) Kozlowski, H.; Luczkowski, M.; Remelli, M.; Valensin, D. *Coord. Chem. Rev.* **2012**, *256*, 2129.
(45) Gazit, E. *FASEB J.* **2002**, *16*, 77.
(46) Kozlowski, H.; Janicka-Klos, A.; Stanczak, P.; Valensin, D.; Valensin, G.; Kulon, K. *Coord. Chem. Rev.* **2008**, *252*, 1069−1078.
(47) Shinchuk, L. M.; Sharma, D.; Blondelle, S. E.; Reixach, N.; Inouye, H.; Kirschner, D. A. *Proteins: Struct., Funct., Bioinf.* **2005**, *61*, 579.
(48) Stranick, S. J.; Weiss, P. S. *Rev. Sci. Instrum.* **1993**, *64*, 1232.
(49) Stranick, S. J.; Weiss, P. S. *Rev. Sci. Instrum.* **1994**, *65*, 918.
(50) Stranick, S. J.; Weiss, P. S. *J. Phys. Chem.* **1994**, *98*, 1762.
(51) Ferris, J. H.; Kushmerick, J. G.; Johnson, J. A.; Youngquist, M. G. Y.; Kessinger, R. B.; Kingsbury, H. F.; Weiss, P. S. *Rev. Sci. Instrum.* **1998**, *69*, 2691.
(52) Voet, D.; Voet, J. G. *Biochemistry*, 2 ed.; John Wiley and Sons, Inc.: New York, 1995.
(53) Nelson, R.; Sawaya, M. R.; Balbirnie, M.; Madsen, A. O.; Riekel, C.; Grothe, R.; Eisenberg, D. *Nature* **2005**, *435*, 773.
(54) Elemans, J. A. A. W.; Lei, S.; De Feyter, S. *Angew. Chem., Int. Ed.* **2009**, *48*, 7298.
(55) Mattson, M. P.; Cheng, B.; Davis, D.; Bryant, K.; Lieberburg, I.; Rydel, R. E. *J. Neurosci.* **1992**, *12*, 376.
(56) Cyr, D. M.; Venkataraman, B.; Flynn, G. W. *Chem. Mater.* **1996**, *8*, 1600.
(57) Bumm, L. A.; Arnold, J. J.; Dunbar, T. D.; Allara, D. L.; Weiss, P. S. *J. Phys. Chem. B* **1999**, *103*, 8122.
(58) Cyr, D. M.; Venkataraman, B.; Flynn, G. W.; Black, A.; Whitesides, G. M. *J. Phys. Chem.* **1996**, *100*, 13747.
(59) Giancarlo, L.; Cyr, D.; Muyskens, K.; Flynn, G. W. *Langmuir* **1998**, *14*, 1465.
(60) Stranick, S. J.; Kamna, M. M.; Weiss, P. S. *Science* **1994**, *266*, 99.
(61) Cygan, M. T.; Dunbar, T. D.; Arnold, J. J.; Bumm, L. A.; Shedlock, N. F.; Burgin, T. P.; Jones, L.; Allara, D. L.; Tour, J. M.; Weiss, P. S. *J. Am. Chem. Soc.* **1998**, *120*, 2721.
(62) Eckert, F.; Leito, I.; Kaljurand, I.; Kuett, A.; Klamt, A.; Diedenhofen, M. *J. Comput. Chem.* **2009**, *30*, 799.
(63) Chen, C. J. *Introduction to Scanning Tunneling Microscopy*, 2nd ed.; Oxford University Press: New York, 2008.
(64) Frisch, M. J.; Trucks, G. W.; Schlegel, H. B.; Scuseria, G. E.; Robb, M. A.; Cheeseman, J. R.; Scalmani, G.; Barone, V.; Mennucci, B.; Petersson, G. A.; Nakatsuji, H.; Caricato, M.; Li, X.; Hratchian, H. P.; Izmaylov, A. F.; Bloino, J.; Zheng, G.; Sonnenberg, J. L.; Hada, M.; Ehara, M.; Toyota, K.; Fukuda, R.; Hasegawa, J.; Ishida, M.; Nakajima, T.; Honda, Y.; Kitao, O.; Nakai, H.; Vreven, T.; Montgomery, J., J. A.; Peralta, J. E.; Ogliaro, F.; Bearpark, M.; Heyd, J. J.; Brothers, E.; Kudin, K. N.; Staroverov, V. N.; Kobayashi, R.; Normand, J.; Raghavachari, K.; Rendell, A.; Burant, J. C.; Iyengar, S. S.; Tomasi, J.; Cossi, M.; Rega, N.; Millam, N. J.; Klene, M.; Knox, J. E.; Cross, J. B.; Bakken, V.; Adamo, C.; Jaramillo, J.; Gomperts, R.; Stratmann, R. E.; Yazyev, O.; Austin, A. J.; Cammi, R.; Pomelli, C.; Ochterski, J. W.; Martin, R. L.; Morokuma, K.; Zakrzewski, V. G.; Voth, G. A.; Salvador, P.; Dannenberg, J. J.; Dapprich, S.; Daniels, A. D.; Farkas, Ö.; Foresman, J. B.; Ortiz, J. V.; Cioslowski, J.; Fox, D. J. *Gaussian 09*, Revision A.1; Gaussian, Inc.: Wallingford, CT, 2009.
(65) Weiss, P. S.; Eigler, D. M. *Phys. Rev. Lett.* **1993**, *71*, 3139.
(66) Moore, A. M.; Yeganah, S.; Yao, Y.; Claridge, S. A.; Tour, J. M.; Ratner, M. A.; Weiss, P. S. *ACS Nano* **2010**, *4*, 7630.
(67) Han, P.; Kurland, A. R.; Giordano, A. N.; Nanayakkara, S. U.; Blake, M. M.; Pochas, C. M.; Weiss, P. S. *ACS Nano* **2009**, *3*, 3115.
(68) Lovell, S. C.; Word, J. M.; Richardson, J. S.; Richardson, D. C. *Proteins: Struct., Funct., Genet.* **2000**, *40*, 389.
(69) Kim, M.; Hohman, J. N.; Cao, Y.; Houk, K. N.; Ma, H.; Jen, A. K.-Y.; Weiss, P. S. *Science* **2011**, *331*, 1312.